

Maximal terahertz emission in high harmonic generation from 3D Dirac semimetals

Jeremy Lim ^{1,3}, Yee Sin Ang^{1,3}, Lay Kee Ang ^{1,3} & Liang Jie Wong ^{2,3}✉

Unlike conventional semiconductor platforms, 3D Dirac semimetals (DSMs) require relatively low input laser intensities for efficient terahertz (THz) high harmonic generation (HHG), making them promising materials for developing compact THz light sources. Here, we show that 3D DSMs' high nonlinearity opens up a regime of nonlinear optics where extreme subwavelength current density features develop within nanoscale propagation distances of the driving field. Our results reveal orders-of-magnitude enhancement in HHG intensity with thicker 3D DSM films, and show that these subwavelength features fundamentally limit HHG enhancement beyond an optimal film thickness. This decrease in HHG intensity beyond the optimal thickness constitutes an effective propagation-induced dephasing. Our findings highlight the importance of propagation dynamics in nanofilms of extreme optical nonlinearity.

¹Science, Maths and Technology, Singapore University of Technology and Design, 8 Somapah Road, Singapore 487372, Singapore. ²School of Electrical and Electronic Engineering, Nanyang Technological University, 50 Nanyang Avenue, Singapore 639798, Singapore. ³These authors contributed equally: Jeremy Lim, Yee Sin Ang, Lay Kee Ang, Liang Jie Wong. ✉email: liangjie.wong@ntu.edu.sg

The terahertz (THz) regime has attracted much attention due to its broad range of potential applications, including electron acceleration^{1–3}, imaging^{4–6}, controlling ultrafast processes in materials^{7–9}, and next-generation communications^{10–12}. These emerging technologies have motivated the quest to realize compact solid-state THz high-harmonic generation (HHG) platforms. The efficiency of HHG, which involves light emission at integer multiples of the input laser frequency, favors materials with strong optical nonlinearity. Three-dimensional Dirac semimetals (3D DSMs)^{13–18}, whose massless charge carriers result in extreme nonlinearity in the THz regime, is one such example. Recent experiments^{19,20} and theory^{21–24} have verified the promise of 3D DSMs in realizing compact, highly efficient THz HHG sources. In particular, even for moderate driving fields of ≤ 10 MV/m, highly efficient generation of the 3rd¹⁹ and up to the 7th²⁰ harmonic have been demonstrated using the 3D DSM Cd₃As₂, with a theoretical study predicting efficient HHG up to the 31st order²³. In contrast, conventional solid-state THz HHG platforms require driving fields ≥ 1 GV/m to generate comparable THz HHG intensities^{25,26}.

Although 2D DSM graphene monolayers have also been shown in both theory^{27–31} and experiments^{32–35} to exhibit extremely high nonlinearities, its atomically thin nature results in a relatively small interaction volume, thereby limiting HHG conversion efficiencies. The finite film thickness of 3D DSMs, which results in a substantially enhanced interaction volume compared to graphene, presents itself as an additional degree-of-freedom through which the THz HHG output can be enhanced—a prospect that remains unexplored.

Here, we show that orders-of-magnitude enhancements of the output THz HHG intensity from 3D DSMs is attainable by increasing the propagation length. Specifically, our results reveal that for a 10 MV/m driving field, the output intensities of the 3rd and 31st harmonics can be enhanced by factors of 144 and 28, respectively in going from a film thickness of 50 nm to 1500 nm. We also show that highly nonlinear materials like 3D DSMs open up a regime of nonlinear optics in which an extremely sub-wavelength phase-flip in the induced current density appears over nanoscale propagation distances—an effect not seen in conventional nonlinear materials. This subwavelength phase-flip results in an optimal thickness for HHG in 3D DSM nanofilms, beyond which the output HHG intensity falls rapidly—an effect which can be understood as an effective propagation-induced dephasing mechanism. Additionally, for fixed field strengths, the optimal film thickness for all harmonics falls within a narrow range of values, indicating that many harmonics can be simultaneously optimized through a single choice of film thickness. Importantly, our result suggests that alternative strategies³⁶ are required to further enhance the HHG output beyond what is possible using 3D DSM films of the optimal thickness. Our findings highlight the importance of accounting for light propagation dynamics in highly nonlinear nanofilms (even beyond 3D DSMs) and pave the way to the development of efficient, solid-state THz light sources and optoelectronics based on 3D DSMs.

Results

When an x -polarized THz pulse impinges upon a 3D DSM film at normal incidence (Fig. 1a), nonlinear currents are induced in the thin film, resulting in the emission of high harmonics. In momentum space (Fig. 1a, inset), the driving laser field induces carrier oscillations within and transitions between the conduction and valence bands, giving rise to intraband and interband currents, respectively, which emit light peaked at integer multiples of the input frequency.

We model the interaction between the externally incident THz pulse and the 3D DSM film by solving Maxwell's equations using

a 1 + 1 D finite-difference time-domain (FDTD) method (see “Methods” section), and determine the induced nonlinear current density $J_x(z, t)$ via nonperturbative quantum theory (Supplementary Note 1). Our approach fully accounts for reflection and transmission at interfaces, pump depletion, and all other effects arising from nonlinear propagation of the combined pump and HHG fields. To confirm that the propagation-induced effects we observe are not a consequence of temperature or scattering, we consider the low-temperature limit ($T \rightarrow 0$ K) and no carrier scattering ($\tau \rightarrow \infty$), although our model can fully account for these effects. Under these conditions, the current density is given by:²³

$$J_x(z, t) = -\frac{ge^2v_x}{6\pi^2\hbar^3v_xv_yv_z}a_x(z, t)[\mathcal{E}_F^2 - \frac{e^2}{5}v_x^2a_x^2(z, t)], \quad ev_x|a_x(z, t)| \leq \mathcal{E}_F$$

$$J_x(z, t) = -\frac{ge\mathcal{E}_F^3}{6\pi^2\hbar^3v_xv_yv_z}\text{sgn}[a_x(z, t)]\left[1 - \frac{\mathcal{E}_F^2}{5e^2v_x^2a_x^2(z, t)}\right], \quad ev_x|a_x(z, t)| > \mathcal{E}_F \quad (1)$$

where we have considered only the intraband current, which dominates when $\hbar\omega \ll 2\mathcal{E}_F$ (\hbar is the reduced Planck's constant, \mathcal{E}_F is the Fermi energy, ω is the driving angular frequency), which is the case we study. Additionally, experiments^{19,20} have shown that the intraband nonlinearities are dominant for high doping values in the THz regime. Specifically, we consider an incident pulse centered at $\omega_0 = 2\pi \times (1 \text{ THz})$ and a Fermi energy $\mathcal{E}_F = 60 \text{ meV}$, which satisfy $\hbar\omega \ll 2\mathcal{E}_F$. In Eq. (1), $g = 4$ is the product of the spin and valley degeneracies, $e > 0$ is the elementary charge, v_i is the 3D DSM's Fermi velocity along the direction $i \in \{x, y, z\}$, and $a_x(z, t) = -e^{-t/\tau} \int_{-\infty}^t e^{t'/\tau} E_x(z, t') dt'$ is the modified vector potential³⁰. When scattering is neglected ($\tau \rightarrow \infty$), which is the case for our simulations, $a_x(z, t)$ reduces to the standard definition of the vector potential: $A_x(z, t) = -\int_{-\infty}^t E_x(z, t') dt'$. We compute the HHG spectra as radiation from the current distribution $J_x(z, t)$. This produces the same results as computing the HHG spectra from the reflected and transmitted electric fields (Supplementary Note 2). We consider the experimentally measured Cd₃As₂ Fermi velocities: $(v_x, v_y, v_z) = (1.28, 1.30, 0.33) \times 10^6 \text{ ms}^{-1}$ ¹³. Our choice of $\mathcal{E}_F = 60 \text{ meV}$ is attainable through chemical doping, and the film thicknesses considered have been realized using molecular beam epitaxy^{19,20,37–41}. Few-cycle THz pulses with peak field strengths similar to those we consider are readily accessible using compact sources^{42–46}. Unless otherwise specified, we use these parameters throughout our work. We emphasize that our method fully incorporates the dispersive induced refractive index through the current density given by Eq. (1).

Figure 1b shows our results for a Cd₃As₂ film driven by an incident 2 ps-long (intensity full-width-at-half-maximum) 1 THz pulse of peak field 10 MV/m (in free space). In going from a film thickness of 50 nm to 1500 nm, we find that the 3rd and 31st harmonics are enhanced by factors of 144 and 28, respectively. However, beyond the optimal thickness of $\approx 1.5 \mu\text{m}$, the output harmonic intensities rapidly diminish with increasing film thickness.

To investigate why the output harmonic intensities decrease beyond a certain film thickness, we plot the 3rd harmonic of the current density, defined as $\text{Re}[\tilde{J}_x(z, \omega) \exp(i\omega t)]$ for $\omega = 3\omega_0$ in Fig. 1c, d for film thicknesses of 1 and 5 μm respectively. Here $\tilde{J}_x(z, \omega)$ is the Fourier transform of $J_x(z, t)$. For a film thickness of 1 μm —thinner than the optimal thickness—we see from Fig. 1c that the current profile undergoes negligible phase shift with propagation distance. Hence, at any given time, the radiation emitted by the current density at different propagation distances constructively interferes. However, for film thicknesses way beyond the optimal value (Fig. 1d), the current density undergoes a π -phase shift across the film. Consequently, the radiation emitted by currents at different z destructively interferes, resulting

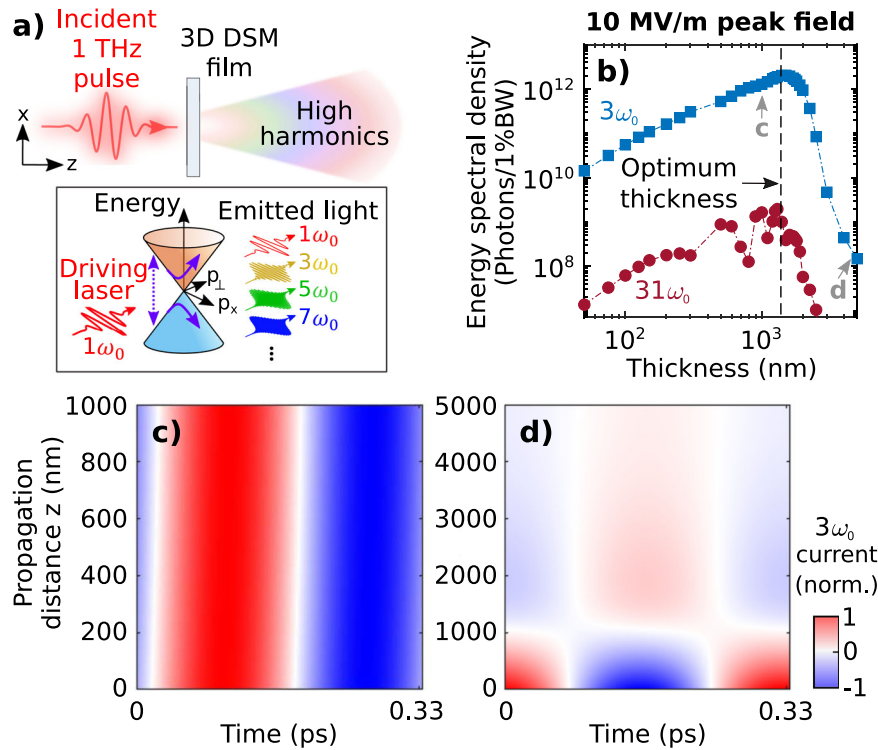


Fig. 1 Propagation-induced limits on HHG in 3D Dirac semimetals (DSMs). **a** An x-polarized laser pulse centered at angular frequency 1 THz impinges on a 3D DSM thin film at normal incidence, resulting in the radiation of higher harmonics. In momentum space $p = (p_{\perp}, p_x)$ (inset), the driving field induces intraband carrier oscillations (solid purple arrows) within and interband carrier transitions (dotted purple arrow) between the valence and conduction bands of the Dirac cone, resulting in the emission of light peaked at odd-integer multiples of the input angular frequency ω_0 . **b** shows orders-of-magnitude enhancements in output intensity with increasing film thickness up to an optimal value of about 1500 nm, beyond which the harmonic output drastically falls. The existence of an optimal thickness arises due to the propagation-induced phase shift of the harmonic current (normalized 3rd harmonic current plotted in **c**, **d**) for 1 μm and 5 μm) across the film thickness. In thinner films **c** the phase shift in the current as a function of propagation distance z is insignificant. Thus, the emitted waves from different z are in-phase and add constructively. For films much thicker than the optimal thickness **d** a π -phase-flip occurs in the current density. The emitted radiation from opposite sides of this phase flip destructively interfere, resulting in the drastic decrease in HHG output with increasing film thickness seen in **(b)**.

in reduced output intensity. It is noteworthy that this phase-flip takes place at an extremely subwavelength propagation distance of 1 μm – 100 times smaller than the driving wavelength. Furthermore, this phase flip also occurs within the skin depth of the 3rd harmonic (about 1.4 μm for scattering times $\tau \sim 150$ fs at $T = 0$ K), which emphasizes the importance of considering these extreme nonlinear propagation dynamics, even for films that are thin enough such that losses from attenuation do not dominate.

While we consider the $\tau \rightarrow \infty$ and $T \rightarrow 0$ K limits here, we show in Supplementary Note 3 that our qualitative conclusions still hold when the effects of finite T and τ are included. In particular, we find that for faster τ down to tens of femtoseconds, the change in the phase of the 3rd harmonic current becomes more gradual as a function of z , and the difference in phase between current components on opposite ends of the film deviates further from π . While this leads to partial cancellation between radiation emitted by current components on opposite ends of the film, the reduction of output HHG intensity is still significant since the 3rd harmonic current still undergoes a net polarity reversal across the film. Additionally, we expect finite temperatures (up to $T = 300$ K) to have a less dominant effect on the nonlinear propagation dynamics relative to finite scattering times that fall within the range of experimentally measured values.

We find that this extreme subwavelength phase-flip only arises within a regime of nonlinear optics where highly nonlinear nanofilms, like 3D DSMs, are involved. We show this in Fig. 2, where the phase shift of the 3rd harmonic current density in a

2500 nm-thick, non-dispersive dielectric film driven by a peak field of 10 MV/m is plotted as a function of its linear and 3rd-order susceptibilities, $\chi^{(1)}$ and $\chi^{(3)}$ respectively. We see that a $\approx \pi$ -phase flip over subwavelength propagation distances only manifests for materials with $\chi^{(3)} \geq 10^{-12} \text{m}^2/\text{V}^2$, such as 3D DSMs. In contrast, conventional materials, which possess relatively small 3rd-order susceptibility by comparison ($\chi^{(3)} \leq 10^{-16} \text{m}^2/\text{V}^2$), see negligible phase shifts over subwavelength thicknesses. See “Supplementary Note 4” for details of the simulations used to plot Fig. 2.

Figure 3 shows the output HHG intensity as a function of film thickness for various harmonics. While the optimal thickness generally differs across harmonics, they lie within a relatively narrow range of values, implying that the output intensity of all harmonics can be simultaneously optimized with a single choice of film thickness. Considering a peak field of 2 MV/m (Fig. 3a), the maximum output intensity for each harmonic is achieved with film thicknesses ranging from 150–300 nm. Considering a peak field of 10 MV/m (Fig. 3b), the optimal film thickness lies between 600 and 1600 nm. The blue shading in Fig. 3a, b indicate these ranges of optimal thicknesses.

We also observe that an increase in optimal film thickness generally accompanies stronger driving fields—a finding that seems unintuitive since larger fields are associated with stronger nonlinearity, which should in turn lead to a smaller optimal film thickness. However, it is important to note that stronger driving fields induce larger harmonic currents, which in turn emit more

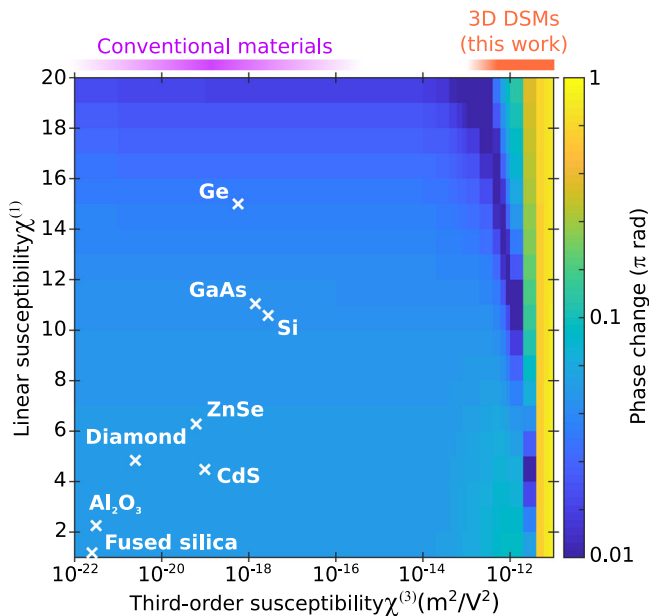


Fig. 2 Extreme subwavelength phase-flip of the induced current in highly nonlinear materials. The colormap shows the phase shift in the 3rd harmonic current for a 2500 nm-thick, non-dispersive dielectric film as a function of its linear and third-order susceptibilities, $\chi^{(1)}$ and $\chi^{(3)}$ respectively, driven by an external field of 10 MV/m. We find that the extreme subwavelength phase-flip of the induced current occurs within a regime of nonlinear optics accessible only by highly nonlinear materials like 3D Dirac semimetals (DSMs); no such phase-flip occurs at extreme subwavelength propagation distances in conventional nonlinear materials, which have weaker nonlinearity ($\chi^{(1)}$ and $\chi^{(3)}$ values⁴⁸ of conventional materials plotted as white crosses). We use the same THz pulse parameters as Fig. 1.

intense HHG. The more intense radiation emitted by the harmonic current components at each z , coupled with a phase flip in the harmonic current that occurs at larger z for stronger fields (Supplementary Fig. S5 in Supplementary Note 5), implies that a larger propagation distance is required to significantly suppress output HHG intensity. This explains why a larger field strength results in a larger optimal film thickness.

Our investigations also reveal that the decrease in output HHG with increasing film thickness can be understood as a propagation-induced dephasing mechanism. We verify this by computing an effective scattering time τ_{eff} in the absence of propagation. In Fig. 4, we show the excellent agreement between the exact spectrum obtained from Maxwell's equations and the spectrum obtained from Eq. (1) fitted to an effective scattering time $\tau = \tau_{\text{eff}}$ while neglecting propagation. Considering an incident pulse with 2 MV/m peak field (Fig. 4a–c), we find that the output spectra for film thicknesses of 800 nm, 1 μm , and 2.5 μm are effectively captured by $\tau_{\text{eff}} = 16.5$ fs, 12.8 fs, and 2.7 fs, respectively. As expected, thicker films (beyond the optimal thickness) correspond to faster scattering times—a trend that holds for a peak field of 10 MV/m (Fig. 4d–f): the spectra for film thicknesses 2 μm , 2.5 μm , and 5 μm are captured by $\tau_{\text{eff}} = 7.5$ fs, 5.1 fs, and 0.2 fs, respectively. Note that these values of τ_{eff} are much shorter than the typical scattering times of $\tau \approx 150$ fs¹⁹ in cleaner samples of Cd_3As_2 , indicating that propagation-induced dephasing is the dominant dephasing mechanism for thicker films. Neglecting propagation effects—to show that the decrease in HHG output can be captured by τ_{eff} —involves assuming a driving field throughout the film that has the same field profile as the irradiated surface. Our procedure finds τ_{eff} such that the area under the spectrum from $2\omega_0$ to $32\omega_0$ is the same as the area under the exact propagated numerical spectrum over the same frequency range.

Discussion

Recent experiments^{19,20} and theory²³ have shown the bulk nature of 3D DSMs enables the output harmonic intensity to exceed the

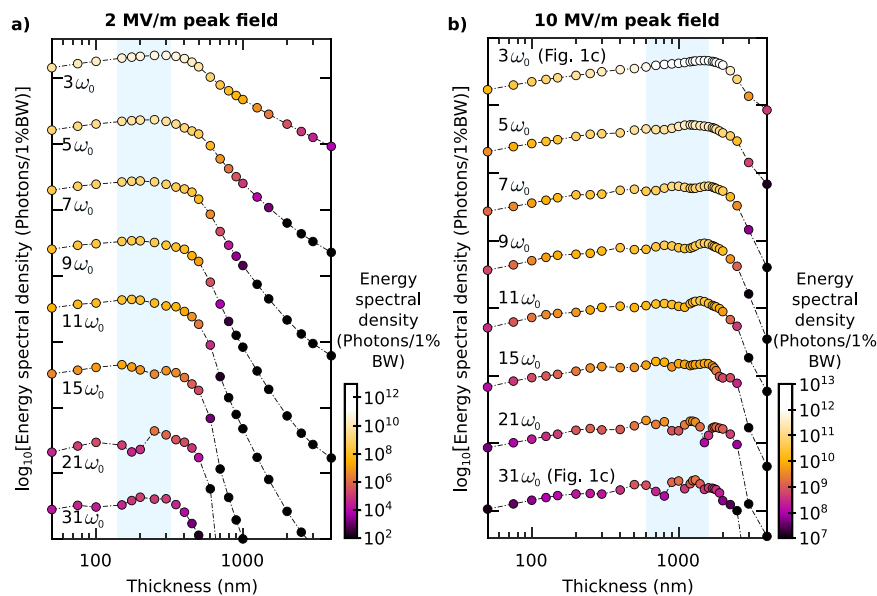


Fig. 3 Optimizing film thickness for HHG in 3D Dirac semimetals (DSMs). **a** For a 3D DSM film driven by a pulse of peak amplitude 2 MV/m and central angular frequency $\omega_0 = 2\pi \times 1$ THz, the optimal thickness for all harmonics falls between 150 and 300 nm. For a larger driving field of 10 MV/m **b** the optimal thickness of all harmonics lies between 600 and 1600 nm. The optimal thicknesses for all harmonics from the 3rd to the 31st lie within the blue shaded areas. The optimal thickness generally shifts to larger values when driven by stronger fields. In both panels, the N th curve from the top has been translated downwards by $10^{4(N-1)}$ for visual clarity; the color of the data points represent their actual magnitudes in units of photons/1% bandwidth (BW). We consider the same parameters as Fig. 1.

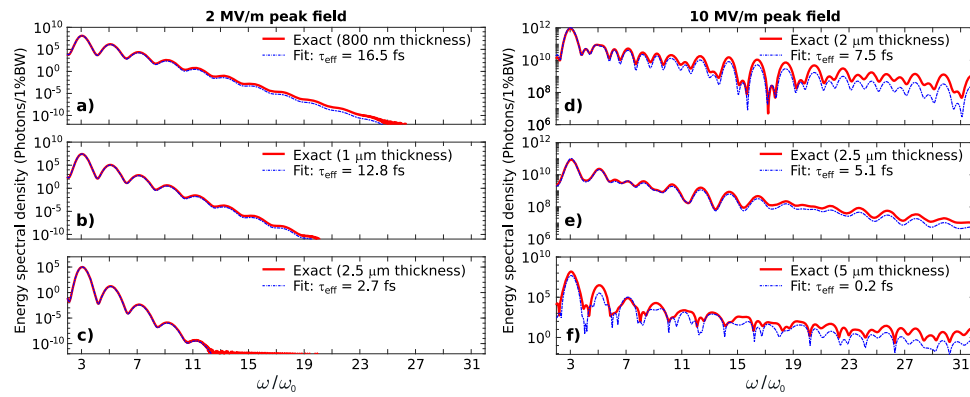


Fig. 4 Effective propagation-induced dephasing in THz HHG. For all panels, we plot the exact output HHG spectrum computed via Maxwell's equations as solid red curves, and the output HHG spectrum computed via Eq. (1) fitted to an effective scattering time τ_{eff} —while neglecting propagation effects—as blue dashed-dotted curves. **a, b, c** show the spectra when 3D DSM films of thicknesses 0.8 μm , 1 μm , and 2.5 μm , respectively are driven by a peak field of 2 MV/m. **d, e, f** show the spectra for film thicknesses of 2 μm , 2.5 μm , and 5 μm respectively, driven by a peak field of 10 MV/m. Our fitted values of τ_{eff} are in good agreement with the exact spectra, implying that the reduced HHG can be captured by an effective dephasing time and is thus due to propagation-induced dephasing effects. As expected, larger film thicknesses correspond to shorter τ_{eff} . We consider the same parameters as in Figs. 1 and 3. Here, we normalize all angular frequencies of the output ω against the fundamental driving frequency ω_0 .

THz HHG output³² from monolayer graphene by over ten times. Importantly, we find that increasing the film thickness beyond previously considered values^{19,20,23} is indeed a promising strategy to further enhance the HHG output intensity by orders of magnitude. However, our studies also reveal that enhancing HHG output intensity through increased film thickness is only possible up to an optimal thickness. We find that using nanofilms of highly nonlinear materials, of which 3D DSMs are only one example, places us within a regime of nonlinear optics in which the induced current undergoes as much as a π -phase-shift over extreme subwavelength propagation distances. This phase-flip results in the existence of an optimal thickness, beyond which the HHG output intensity falls. We show that this decrease in HHG intensity can be captured by an effective propagation-induced dephasing time τ_{eff} . It is noteworthy that this propagation-induced dephasing occurs even over extremely subwavelength propagation lengths of ~ 100 nm to ~ 1 μm —about 100–1000 times shorter than the central driving wavelength. In contrast, a recent theoretical study⁴⁷ has shown that propagation-induced dephasing in conventional materials, which have weaker nonlinearity, only becomes significant when the film thickness far exceeds the central driving wavelength. We emphasize that their result is entirely consistent with our findings presented in this work: in conventional nonlinear materials, negligible phase-change of the induced current occurs over extreme subwavelength propagation distances, which in turn results in negligible propagation-induced dephasing on subwavelength scales. These observations are in line with conventional nonlinear optical theory, which tells us that nonlinear propagation effects become significant over a characteristic length scale that falls inversely with the nonlinear susceptibility:⁴⁸ $L \propto 1/(\omega_0 \chi^{(3)})$. Additionally, as a result of a large $\chi^{(3)}$, frequency up-conversion is extremely efficient, leading to strong high-harmonic fields, which themselves accumulate significant nonlinear effects over even shorter propagation lengths (since $L \propto 1/\omega_0$). This explains why propagation-induced dephasing in conventional nonlinear materials is only expected for film thicknesses far exceeding the central driving wavelength. Our study thus establishes the important role of light propagation effects on extreme subwavelength distances in this regime of nonlinear optics where highly nonlinear materials—such as emerging topological semimetals beyond 3D DSMs^{49–58}, for instance—are considered.

Importantly, our results suggest that restrictions on the optimal film thickness may be circumvented by using various metamaterial configurations. For instance, a recent experiment³⁶ demonstrated orders-of-magnitude enhancement in the THz harmonic output from a graphene-photonic grating metamaterial relative to the output from a graphene monolayer—a result enabled by the field enhancement from the grating. Platforms that combine 3D DSM films with similar photonic structures could be a promising method allowing for greater enhancements of THz HHG output beyond what is fundamentally permitted by a single 3D DSM layer. An alternative metamaterial configuration would be a superlattice of 3D DSM nanofilms (e.g., 1D array of 3D DSM films) interleaved with other materials (e.g., metals or dielectrics). This could be useful since 3D DSMs nanostructured in this manner could also be used to enhance the output HHG intensity even beyond the optimal film thickness in a single-layer unstructured 3D DSM film. These 3D DSM superlattices would also introduce additional versatility to the output HHG spectrum, for instance, to selectively amplify or attenuate specific harmonics, enabling on-demand THz light-shaping on a chip-scale platform.

Conclusions

In summary, we have shown that the output intensity of THz HHG in 3D DSMs can be enhanced by orders of magnitude with increased propagation length. Additionally, we find that using nanofilms made of highly nonlinear materials like 3D DSMs opens up a regime of nonlinear optics where extremely subwavelength features develop in the induced current density, an effect that is negligible in conventional nonlinear materials. The phase-flip in current density results in the destructive interference of emitted radiation from different parts of the film. We verify that this phenomenon constitutes propagation-induced dephasing of the HHG process by computing an effective dephasing time τ_{eff} for light generation in 3D DSMs. We also show that the optimal film thickness for all output harmonics lies within a relatively narrow range for a given driving field, and that this optimal film thickness generally increases for stronger fields. Our findings highlight the importance of including pulse propagation effects for highly nonlinear materials, including 3D DSMs and other bulk topological semimetals. Furthermore, our findings

suggest that appropriate nanostructuring could enable still-greater THz HHG output efficiency to be achieved. Our work paves the way to efficient solid-state THz light sources and optoelectronics based on highly nonlinear material platforms like 3D DSMs.

Methods

Numerical simulation of 3D DSM thin-film interaction with a THz pulse. To model the interaction of a driving THz pulse linearly polarized along x with a finite 3D DSM thin film at normal incidence, we employ a (1 + 1)D finite-difference time-domain (FDTD) routine that fully incorporates all nonlinear propagation effects of the combined pump and higher-harmonic field, as well as reflection and transmission at interfaces. At the simulation box edge $z = z_{\text{in}}$, we have the input fields $\mathbf{E}_{\text{in}} = (E_{\text{in},x}, 0, 0)$ and $\mathbf{H}_{\text{in}} = (0, E_{\text{in},x}/\eta_0, 0)$, where η_0 is the free space impedance and $E_{\text{in},x}$ is given by a plane wave with a Poisson power spectrum:⁵⁹

$$E_{\text{in},x}(z_{\text{in}}, t) = \text{Re} \left\{ E_{x,0} e^{i\phi_0} \left[1 - \frac{i(k_0 z' - \omega_0 t)}{s} \right]^{-s-1} \right\}, \quad (2)$$

where $k_0 = \omega_0/c$ is the free-space light wavenumber, c is the speed of light in free space, ϕ_0 is a phase constant, and $s > 0$ is a real parameter that determines the pulse duration (we use $s = 56.4$ throughout our work, which corresponds to an intensity full-width at half-maximum (FWHM) pulse duration of ≈ 2 ps). We define $z' = z_{\text{in}} - z_{\text{pk}}$, where z_{pk} is the initial pulse peak location. We note that a plane wave input pulse and a (1 + 1)D FDTD neglects effects like beam diffraction and wavefront curvature (as opposed to a focused laser pulse and a (3 + 1)D FDTD). However, for a weakly focused laser pulse (even one of the high field strengths), a plane wave pulse is a reasonable approximation.

We proceed to write Maxwell's equations in the form

$$\partial_t H_y(z, t) = -\frac{1}{\mu} \partial_z E_x(z, t), \quad \epsilon_0 \partial_t E_x(z, t) = -\partial_z H_y(z, t) - J_x(z, t). \quad (3)$$

The total current is the sum $J_x = J_x^f + J_x^p$, where J_x^f is the free current and $J_x^p = \partial_z P_x$ is the current arising from the dielectric polarization P_x . Discretizing these equations on a Yee grid and defining normalized time and spatial steps $\Delta(\omega_0 t)$ and $\Delta(k_0 z)$ respectively, we obtain

$$\begin{aligned} cB_y|_{j+1/2}^{n+1/2} &= cB_y|_{j+1/2}^{n-1/2} - \frac{\Delta(\omega_0 t)}{\Delta(k_0 z)} (E_x|_{j+1}^n - E_x|_j^n) \\ E_x|_j^{n+1} &= E_x|_j^n - \frac{1}{\mu_r} \frac{\Delta(\omega_0 t)}{\Delta(k_0 z)} \left(cB_y|_{j+1/2}^{n+1/2} - cB_y|_{j-1/2}^{n+1/2} \right) - \frac{\Delta(\omega_0 t)}{\omega_0 \epsilon_0} J_x|_j^{n+1} \end{aligned} \quad (4)$$

We assume that the material is linear and homogeneous in magnetic field response: $B_y = \mu_0 \mu_r H_y$ ($\mu_r = 1$ throughout our work). The upper index n denotes the time step. The lower index j refers to the spatial grid position. Note that $J_x|_j^{n+1}$ makes this scheme implicit because the current depends on the field $E_x|_j^{n+1}$ at the current time step. To obtain the self-consistent $J_x|_j^{n+1}$ and $E_x|_j^{n+1}$, we adopt a fixed-point iteration method in which $J_x|_j^{n+1} = J_x|_j^n$ (i.e., the previous time step value) is used as an initial guess to compute $E_x|_j^{n+1}$. We use this first pass solution to obtain a refined approximation of $J_x|_j^{n+1}$. This procedure is iterated until the error between two consecutively refined values of $E_x|_j^{n+1}$ is within a specified tolerance. We assume free space on either side of the 3D DSM film and implement Mur absorbing boundary conditions⁶⁰ at both ends of our FDTD grid. In the limit $\hbar\omega_0 \ll 2\mu$ (where μ is the chemical potential) and finite temperatures, $J_x(z, t)$ is computed using Eq. (S14) in Supplementary Note 1. When $T \rightarrow 0$ K, we compute $J_x(z, t)$ using main text Eq. (1).

The HHG spectrum in terms of the energy spectral density can then be computed from the numerical solution of $J_x(z, t)$ using:

$$\text{HHG spectrum} = \frac{dU}{d\omega} = \int_0^{2\pi} \int_0^{\pi/2} \frac{d^2 U}{d\omega d\Omega} \sin\theta d\theta d\phi, \quad (5)$$

where $d^2 U/d\omega d\Omega$, which denotes the energy U radiated into a unit solid angle Ω and unit angular frequency ω in the far-field, takes the following form:²³

$$\frac{d^2 U}{d\omega d\Omega} = \frac{A^2}{8\pi^3 \epsilon_0 c} (\cos^2 \phi \cos^2 \theta + \sin^2 \phi) \left| i k e^{-ikr} J_1(kR \sin \theta) \int_0^D \bar{J}_x(z', \omega) e^{ikz' \cos \theta} dz' \right|^2. \quad (6)$$

Here, $A = \pi R^2$ is the area of the circular radiating region of radius R , θ is the polar angle (with respect to forward propagation directions), ϕ is the azimuthal angle, $k = \omega/c$ is the wavenumber, J_1 is the first-order Bessel function, r is the radial position to the observer, D is the film thickness, and $\bar{J}_x(z', \omega)$ is the Fourier transform of $J_x(z', t)$. The integral is taken with respect to the source coordinate z' . Note that the current J_x is assumed to be uniform in the transverse (x, y) directions. We consider $R = 1$ mm for all cases presented in our work.

Data availability

The simulation results presented in this paper are available from the corresponding author on reasonable request.

Code availability

The custom computer code used to generate the results is the 1+1 D finite-difference time-domain scheme described in the "Methods" section.

Received: 18 June 2021; Accepted: 14 October 2021;

Published online: 03 November 2021

References

- Zhang, D. et al. Cascaded multicycle terahertz-driven ultrafast electron acceleration and manipulation. *Phys. Rev. X* **10**, 011067 (2020).
- Nanni, E., Huang, W. & Hong, K. H. Terahertz-driven linear electron acceleration. *Nat. Commun.* **6**, 8486 (2015).
- Sharma, A., Tibai, Z. & Fulop, J. A. Terahertz-driven wakefield electron acceleration. *J. Phys. B: Mol. Opt. Phys.* **51**, 204001 (2018).
- Cocker, T. et al. An ultrafast terahertz scanning tunnelling microscope. *Nat. Photon.* **7**, 620–625 (2013).
- Stantchev, R. I. et al. Real-time terahertz imaging with a single-pixel detector. *Nat. Commun.* **11**, 2535 (2020).
- Wu, X., Lu, H. & Sengupta, K. Programmable terahertz chip-scale sensing interface with direct digital reconfiguration at sub-wavelength scales. *Nat. Commun.* **10**, 2722 (2019).
- Kampfrath, T. et al. Coherent terahertz control of antiferromagnetic spin waves. *Nat. Photon* **5**, 31–34 (2011).
- Kampfrath, T., Tanaka, K. & Nelson, K. Resonant and non-resonant control over matter and light by intense terahertz transients. *Nat. Photon* **7**, 680–690 (2013).
- Zaks, B., Liu, R. & Sherwin, M. Experimental observation of electron-hole recollisions. *Nature* **483**, 580–583 (2012).
- Nagatsuma, T., Ducournau, G. & Renaud, C. Advances in terahertz communications accelerated by photonics. *Nat. Photon* **10**, 371–379 (2016).
- Zhang, Q. et al. Collective nonperturbative coupling of 2D electrons with high-quality-factor terahertz cavity photons. *Nat. Phys.* **12**, 1005–1011 (2016).
- Yang, Y. et al. Terahertz topological photonics for on-chip communication. *Nat. Photon* **14**, 446–451 (2020).
- Liu, Z. K. et al. A stable three-dimensional topological Dirac semimetal Cd_3As_2 . *Nat. Mater.* **13**, 677–681 (2014).
- Liu, Z. K. et al. Discovery of a three-dimensional topological Dirac semimetal, Na_3Bi . *Science* **343**, 864–867 (2014).
- Borisenko, S. et al. Experimental realization of a three-dimensional Dirac semimetal. *Phys. Rev. Lett.* **113**, 027603 (2014).
- Neupane, M. et al. Observation of a three-dimensional topological Dirac semimetal phase in high-mobility Cd_3As_2 . *Nat. Commun.* **5**, 3786 (2014).
- Zheng, G. et al. Transport evidence for the three-dimensional Dirac semimetal phase in ZrTe_5 . *Phys. Rev. B* **93**, 115414 (2016).
- Novak, M., Sasaki, S., Segawa, K. & Ando, Y. Large linear magnetoresistance in the Dirac semimetal TlBiSe . *Phys. Rev. B* **91**, 041203 (2015).
- Cheng, B. et al. Efficient terahertz harmonic generation with coherent acceleration of electrons in the Dirac semimetal Cd_3As_2 . *Phys. Rev. Lett.* **124**, 117402 (2020).
- Kovalev, S. et al. Non-perturbative terahertz high-harmonic generation in the three-dimensional Dirac semimetal Cd_3As_2 . *Nat. Commun.* **11**, 2451 (2020).
- Ooi, K. J. A. et al. Nonlinear plasmonics of three-dimensional Dirac semimetals. *APL Photon* **4**, 034402 (2019).
- Zhang, T., Ooi, K. J. A., Chen, W., Ang, L. K. & Ang, Y. S. Optical Kerr effect and third harmonic generation in topological Dirac/Weyl semimetal. *Opt. Express* **27**, 38270–38280 (2019).
- Lim, J. et al. Efficient generation of extreme terahertz harmonics in three-dimensional Dirac semimetals. *Phys. Rev. Res.* **2**, 043252 (2020).
- Cheng, J. L., Sipe, J. E., & Wu, S. W. Third-order optical nonlinearity of three-dimensional massless Dirac fermions. *ACS Photon.* **7**, 2515–2526 (2020).
- Schubert, O. et al. Sub-cycle control of terahertz high-harmonic generation by dynamical Bloch oscillations. *Nat. Photon* **8**, 119–123 (2014).
- Hohenleutner, M. et al. Real-time observation of interfering crystal electrons in high-harmonic generation. *Nature* **523**, 572–575 (2015).
- Wright, A. R., Xu, X. G., Cao, J. C. & Zhang, C. Strong nonlinear optical response of graphene in the terahertz regime. *Appl. Phys. Lett.* **95**, 072101 (2009).
- Ishikawa, K. L. Nonlinear optical response of graphene in time domain. *Phys. Rev. B* **82**, 201402 (2010).
- Shareef, S., Ang, Y. S. & Zhang, C. Room-temperature strong terahertz photon mixing in graphene. *J. Opt. Soc. Am. B* **29**, 274–279 (2012).

30. Marini, A., Cox, J. D. & García de Abajo, F. J. Theory of graphene saturable absorption. *Phys. Rev. B* **95**, 125408 (2017).
31. Cox, J. D., Marini, A. & García de Abajo, F. J. Plasmon-assisted high-harmonic generation in graphene. *Nat. Commun.* **8**, 1–7 (2017).
32. Hafez, H. A. et al. Extremely efficient terahertz high-harmonic generation in graphene by hot Dirac fermions. *Nature* **561**, 507–511 (2018).
33. Soavi, G. et al. Broadband, electrically tuneable third-harmonic generation in graphene. *Nat. Nanotechnol.* **13**, 583–588 (2018).
34. Baudisch, M. et al. Ultrafast nonlinear optical response of Dirac fermions in graphene. *Nat. Commun.* **9**, 567 (2018).
35. Soavi, G. Hot electrons modulation of third-harmonic generation in graphene. *ACS Photon* **6**, 2841–2849 (2019).
36. Deinert, J.-C. et al. Grating-graphene metamaterial as a platform for terahertz nonlinear photonics. *ACS Nano* **15**, 11451154 (2021).
37. Neubauer, D. et al. Interband optical conductivity of the [001]-oriented Dirac semimetal Cd₃As₂. *Phys. Rev. B* **93**, 121202 (2016). (R).
38. Yuan, X. et al. Direct observation of Landau level resonance and mass generation in Dirac semimetal Cd₃As₂ thin films. *Nano Lett.* **17**, 2211–2219 (2017).
39. Nishihaya, S. et al. Quantized surface transport in topological Dirac semimetal films. *Nat. Commun.* **10**, 2564 (2019).
40. Nishihaya, S. et al. Gate-tuned quantum hall states in Dirac semimetal (Cd_{1-x}Zn_x)₃As₂. *Sci. Adv.* **4**, eaar5668 (2018).
41. Liang, T. et al. Anomalous Nernst effect in the Dirac semimetal Cd₃As₂. *Phys. Rev. Lett.* **118**, 136601 (2017).
42. Hirori, H., Doi, A., Blanchard, F. & Tanaka, K. Single-cycle terahertz pulses with amplitudes exceeding 1 MV/cm generated by optical rectification in LiNbO₃. *Appl. Phys. Lett.* **98**, 091106 (2011).
43. Hauri, C. P., Ruchert, C., Vicario, C. & Ardana, F. Strong-field single-cycle THz pulses generated in an organic crystal. *Appl. Phys. Lett.* **99**, 161116 (2011).
44. Huang, S. W. et al. High conversion efficiency, high energy terahertz pulses by optical rectification in cryogenically cooled lithium niobate. *Opt. Lett.* **38**, 796–798 (2013).
45. Fulop, J., Palfalvi, L., Hoffmann, M. C. & Hebling, J. Towards generation of mJ-level ultrashort THz pulses by optical rectification. *Opt. Express* **19**, 15090–15097 (2011).
46. Fulop, J., Palfalvi, L., Almasi, G. & Hebling, J. Design of high-energy terahertz sources based on optical rectification. *Opt. Express* **18**, 12311–12327 (2010).
47. Kilen, I. et al. Propagation induced dephasing in semiconductor high-harmonic generation. *Phys. Rev. Lett.* **125**, 083901 (2020).
48. Boyd, R. W. (eds) *Nonlinear Optics* (Academic Press, 2020).
49. Yan, M. et al. Lorentz-violating type-II Dirac fermions in transition metal dichalcogenide PtTe₂. *Nat. Commun.* **8**, 257 (2017).
50. Li, S. et al. Type-II nodal loops: Theory and material realization. *Phys. Rev. B* **96**, 081106 (2017).
51. Zhang, K. et al. Experimental evidence for type-II Dirac semimetal in PtSe₂. *Phys. Rev. B* **96**, 125102 (2017).
52. Huang, H., Zhou, S. & Duan, W. Type-II Dirac fermions in the PtSe₂ class of transition metal dichalcogenides. *Phys. Rev. B* **94**, 121117 (2016).
53. Li, P. et al. Evidence for topological type-II Weyl semimetal WTe₂. *Nat. Commun.* **8**, 2150 (2017).
54. Li, S. et al. Almost ideal nodal-loop semimetal in monoclinic CuTeO₃ material. *Phys. Rev. B* **97**, 245148 (2018).
55. Zhao, Z., Hang, Y., Zhang, Z. & Guo, W. Topological hybrid nodal-loop semimetal in a carbon allotrope constructed by interconnected Riemann surfaces. *Phys. Rev. B* **100**, 115420 (2019).
56. Zhang, X. et al. Hybrid nodal loop metal: unconventional magnetoresistance and material realization. *Phys. Rev. B* **97**, 125143 (2018).
57. Zhou, Y., Xiong, F., Wan, X. & An, J. Hopf-link topological nodal-loop semimetals. *Phys. Rev. B* **97**, 155140 (2018).
58. Lee, C. H. et al. Enhanced higher harmonic generation from nodal topology. *Phys. Rev. B* **102**, 035138 (2020).
59. Feng, S. & Winful, H. G. Spatiotemporal structure of isodiffracting ultrashort electromagnetic pulses. *Phys. Rev. E* **61**, 862 (2000).
60. Mur, G. Absorbing boundary conditions for the finite difference approximation of the time-domain electromagnetic-field equations. *IEEE Trans. Electromagn. Compat.* **23**, 377 (1981).

Acknowledgements

L.J.W. acknowledges the support of the Agency for Science, Technology, and Research (A*STAR) Advanced Manufacturing and Engineering Young Individual Research Grant (A1984c0043); and the Nanyang Assistant Professorship Start-up Grant. J.L. and L.K.A. acknowledge funding from Singapore MOE Tier 2 Grant (2018-T2-1-007), MOE PhD RSS, and USA ONRG grant (N62909-19-1-2047). Y.S.A. acknowledges funding from SUTD Start-up Research Grant.

Author contributions

J.L. developed the theory and performed the simulations. J.L. and L.J.W. conceived the idea, analysed the results and wrote the manuscript with inputs from Y.S.A. and L.K.A. L.J.W. supervised the project.

Competing interests

The authors declare no competing interests.

Additional information

Supplementary information The online version contains supplementary material available at <https://doi.org/10.1038/s42005-021-00738-6>.

Correspondence and requests for materials should be addressed to Liang Jie Wong.

Peer review information *Communications Physics* thanks Klaas-Jan Tielrooij and the other anonymous reviewer(s) for their contribution to the peer review of this work. Peer reviewer reports are available.

Reprints and permission information is available at <http://www.nature.com/reprints>

Publisher's note Springer Nature remains neutral with regard to jurisdictional claims in published maps and institutional affiliations.



Open Access This article is licensed under a Creative Commons Attribution 4.0 International License, which permits use, sharing, adaptation, distribution and reproduction in any medium or format, as long as you give appropriate credit to the original author(s) and the source, provide a link to the Creative Commons license, and indicate if changes were made. The images or other third party material in this article are included in the article's Creative Commons license, unless indicated otherwise in a credit line to the material. If material is not included in the article's Creative Commons license and your intended use is not permitted by statutory regulation or exceeds the permitted use, you will need to obtain permission directly from the copyright holder. To view a copy of this license, visit <http://creativecommons.org/licenses/by/4.0/>.

© The Author(s) 2021